Fuel 328 (2022) 125372

Contents lists available at ScienceDirect

Fuel

journal homepage: www.elsevier.com/locate/fuel

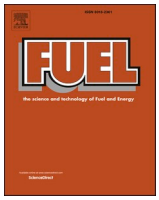

Full Length Article

# Inlet pulsation-induced extinction and plasma-assisted stabilization of premixed swirl flames

Jinguo Sun [a], Wei Cui [a,b], Yong Tang [a,c], Chendong Kong [d], Shuiqing Li [a,*]

[a] Key Laboratory for Thermal Science and Power Engineering of Ministry of Education, Department of Energy and Power Engineering, Tsinghua University, Beijing 100084, China
[b] School of Mechanical Engineering, Xi'an Jiaotong University, Xi'an 710049, China
[c] School of Aerospace Engineering, Beijing Institute of Technology, Beijing 100081, China
[d] Institute of Thermal Energy Engineering, Shanghai Jiao Tong University, Shanghai 200240, China

ARTICLE INFO

*Keywords:*
Extinction
Pulsed plasma discharge
Flow pulsation disturbance
Simultaneous OH-PLIF/PIV
Decoupled simulation of LES and ZDPlasKin

ABSTRACT

This paper intensively investigates the inlet pulsation-induced extinction of a premixed swirl flame (PSF) and its plasma-assisted stabilization using the microsecond repetitively pulsed (MRP) discharge. A well-designed low-frequency flow pulsation is applied to the air feedline for the mimicking of transient operations/disturbances in practical engines, which exhibits significant deterioration on the lean blowout (LBO) limit. The MRP discharge is utilized to improve the stability of perturbed flames. It extends the LBO limit at a proper time delay between the air flow pulsation and the discharge, with discharge power less than 1% of the combustion power. Further, the validated large-eddy simulations (LES) and the simultaneous OH planar laser-induced fluorescence/particle imaging velocimetry (OH-PLIF/PIV) measurements are performed to capture the unsteady evolution of flames approaching lean blowout. The nonlinear flame response to the flow pulsation quantitatively reveals the phase difference between the maximum local stretch rates ($\kappa_{max}$) and volumetric heat release rates ($\dot{q}_c$). A combined effect of the excessive stretch and the reduction of heat release due to flow pulsation can be used to interpret the flame extinction. Finally, a novel LES-ZDPlasKin combined approach, which decouples the discharge and combustion processes, is dexterously developed to simulate plasma-assisted combustion behaviors. The reignition and stabilization due to the plasma effects are well reproduced in the predictive model, pronouncing the indispensable and synergistic thermal and kinetic effects of the MRP discharge on flame stabilization.

## 1. Introduction

In the development of advanced combustion and propulsion applications, growing demands for higher power outputs, more flexible operating ranges, and lower pollutant emissions reinforce widespread concerns about flame stabilities, which require not only comprehensive understandings of the underlying mechanisms but also more effective control strategies [1–5]. Flame stabilities are classified into two categories: dynamic and static stabilities [6,7]. The dynamic stability problem related to self-excited thermoacoustic oscillation, usually resulting from the in-phase high/medium frequency harmonic fluctuations in pressure and heat release rate, was extensively studied [8–10]. Some groundbreaking findings were reviewed in references [3,11]. However, less emphasis has been given to the static instability, i.e., the blowout caused by the abrupt changes in operating conditions, despite its frequent occurrences in practical combustors, such as ramjets, afterburners, and rocket motors [12–14].

The loss of static flame stabilities under transient operations poses a significant threat to the performance and safety of the combustor. Taking the aircraft engine as an example, more than half of the aviation accidents over the past decade have occurred during the flight phases of descent, approach, and landing [15]. Such operational transients bring about low-frequency, large-amplitude disturbances in fuel and oxidant flows, causing severe damage to static flame stabilities and even overall combustion failures. Cohen et al. designed a unique facility to evaluate the operability of gas turbine combustors during transient events [12,16]. Nevertheless, the flame response to such pulsation disturbances is scarcely reported, which is a primary motivation of this work.

In addition, seeking effective strategies to control the above-mentioned instability has always been another priority for the

* Corresponding author.
*E-mail address:* lishuiqing@tsinghua.edu.cn (S. Li).

https://doi.org/10.1016/j.fuel.2022.125372
Received 5 June 2022; Received in revised form 16 July 2022; Accepted 19 July 2022
Available online 27 July 2022

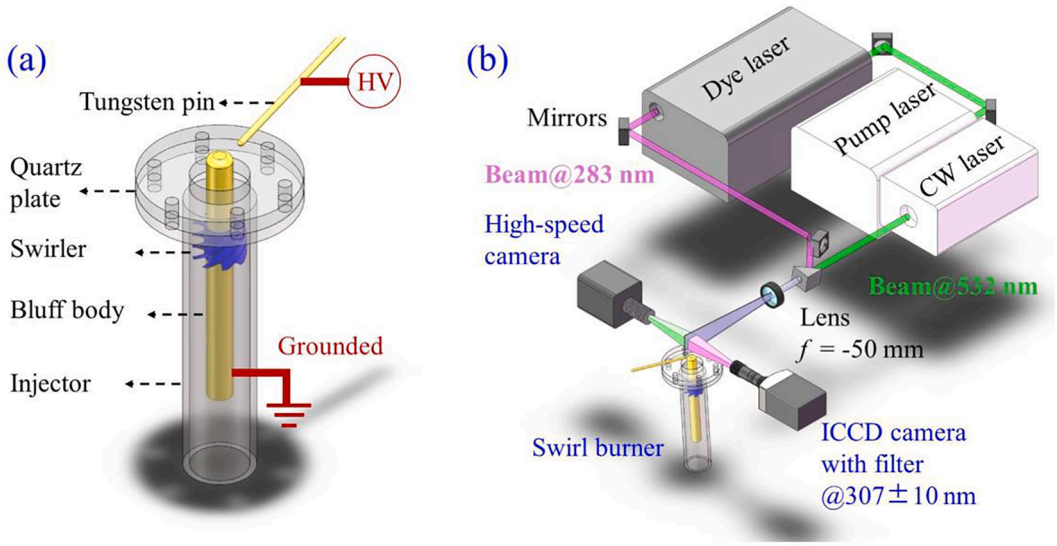


**Fig. 1.** Schematics of (a) the pulsed discharge reactor and (b) simultaneous OH-PLIF/PIV system.

combustion community. Passive control strategies for stabilizing premixed combustion in gas turbines, including control model concepts, simple time-lag models, and acoustic dampers, were summarized in the literature [17]. Traditional active control theories and methods involving perturbing specific combustion parameters such as inlet velocity were reviewed in [4,5,18]. Over the past decade, there has been high interest in a novel technology of plasma-assisted combustion (PAC) in the search for effective ways to improve ignition and stabilization performances [19–32]. Plasma was applied not only to suppress the thermoacoustic oscillations, but also to extend the blowout limits [30].

More recently, we designed a low-frequency air flow pulsation system to trigger static instabilities in premixed swirl flames, and found that the lean blowout (LBO) limits of perturbed flames were significantly deteriorated [33]. In this work, the OH planar laser-induced fluorescence (OH-PLIF) and CH* chemiluminescence were measured to illustrate dynamics of the entire flame approaching blowout. However, due to the lack of quantification of the instantaneous flow structure, the temporal variation of localized flame extinction caused by the flow pulsation remains unknown. Hence, the first purpose of the present study is to establish simultaneous OH-PLIF and particle imaging velocimetry (PIV) measurement system to visualize the unsteady flame and flow dynamics near blowout. Furthermore, a numerical model based on large-eddy simulation (LES) are developed and validated to quantitatively analyze the dynamic responses of PSFs to inlet pulsations.

To overcome the flow pulsation, the previous work [33] applied a microsecond repetitively pulsed (MRP) discharge to alter the perturbed swirl flames. Results showed that the LBO limit was extended by the reignition effect of MRP discharges at a proper time delay between the discharge and flow pulses. However, the multi-scale nature of plasma-assisted combustion makes it rather challenging to quantitatively decouple the complicated effects of MRP discharges on combustion, particularly for perturbed swirl flames. Thus, based on the validated LES simulation, the second purpose of this study is to develop a new approach to decouple the combustion and the discharge processes by combining the LES model and ZDPlasKin package [34], and further elucidate different pathways of plasma to enhance combustion in perturbed swirl flames.

## 2. Experimental setup

### 2.1. Swirl burner, flow pulsation, and plasma discharge

Fig. 1a shows a schematic of a premixed swirl burner integrated with a microsecond repetitively pulsed discharge system. The burner consists of an 18 mm diameter ($d_i$) injector, an 8 mm diameter ($d_c$) cylindrical bluff body, and a vane swirler with a blade inclination angle of $\alpha = 45$ degrees. The pre-mixture passing through the swirler forms a swirling flow with a swirl number ($Sw$) of 0.75, which is determined by the formula [35]:

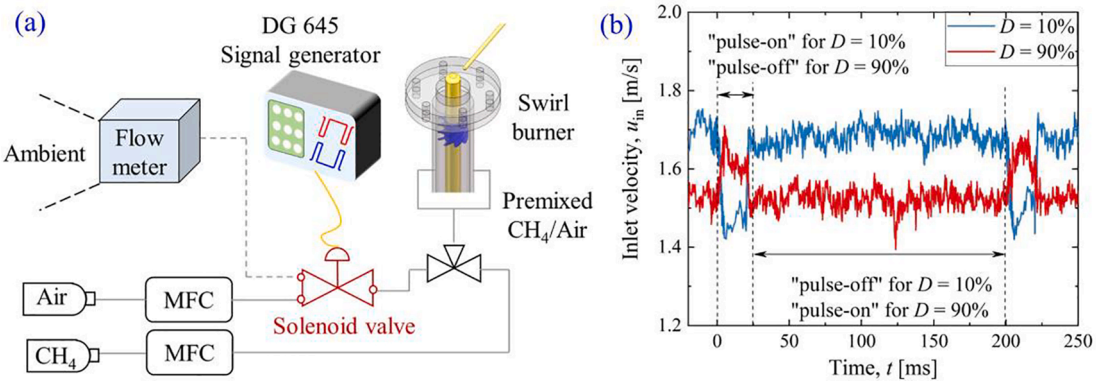


**Fig. 2.** (a) A schematic of the air flow pulsation generation system; (b) LDV-characterized velocity profiles of non-reacting jet flows under negative and positive pulsations.

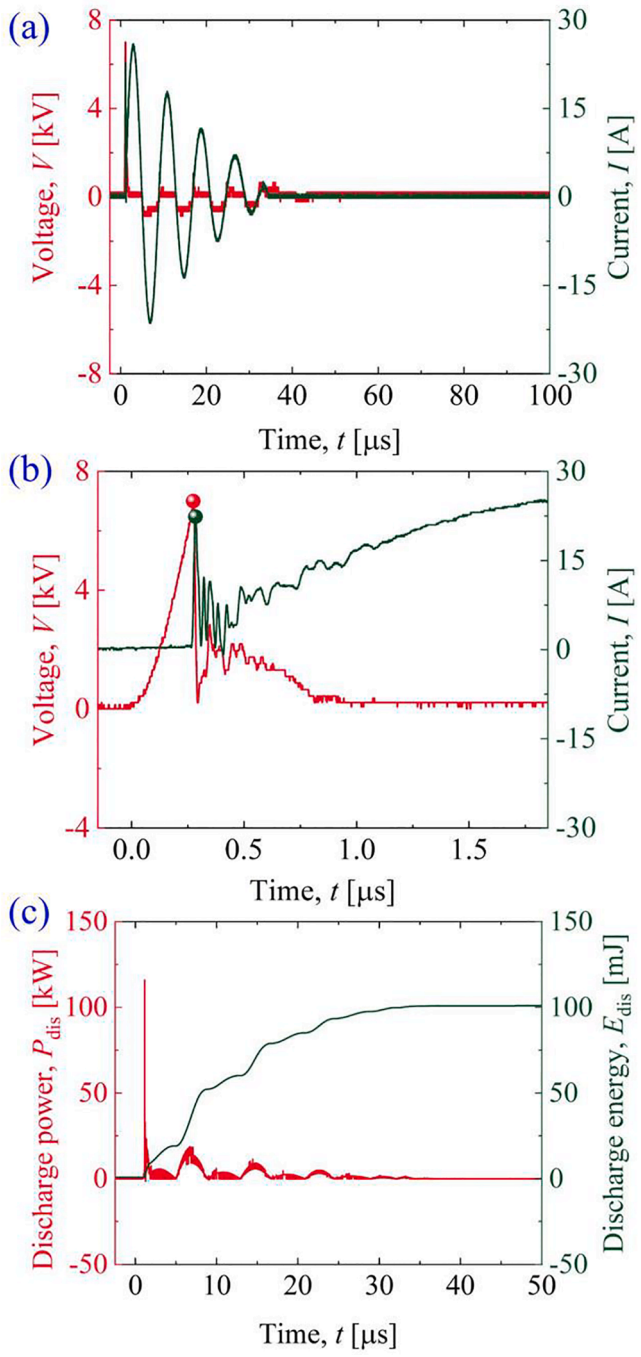


**Fig. 3.** Waveforms of (a) the voltage and current, (b) a zoom-in graph, and (c) temporal power and energy deposition of the MRP discharge.

$$Sw = \frac{2}{3}\tan(\alpha)\frac{1-(d_c/d_i)^3}{1-(d_c/d_i)^2} \quad (1)$$

A 1 mm diameter tungsten pin is connected to a homemade microsecond pulsed power supply (CMPC-40D) and mounted 20 mm above the nozzle outlet to serve as the high-voltage electrode. The coaxial bluff body is grounded. The distance between the pin rim and the bluff body is around 6 mm for an optimal discharge. In addition to the efficient generation of MRP discharge, the concise configuration also ensures the minimal impact on the flame itself, verified by comparing the LBO limits and flame structures with and without this small-size pin. To avoid undesirable discharges between the nozzle outlet and the pin, a 5 mm thick quartz plate on the nozzle outlet serves as an insulator.

A digital control system is specifically designed to generate low-frequency flow pulsations from the air pipeline. As shown in Fig. 2a, the system consists of a pulse delay generator (Stanford Research Systems, Model DG645) and a fast-acting solenoid valve (MAC35A-ACA) connected to the mainstream air pipeline. Quasi-rectangle signals delivered by DG645 control the valve as follows: when the voltage signal is logical high (pulse-on stage), the valve opens and allows a small amount of air to leak into the environment, leading to a large-amplitude flow pulsation. The repetition rate of the flow pulsation is set to 5 Hz, much lower than the cut-off frequency of the flame as a low-pass filter [36]. The ratio of the pulse-on duration ($t_{\text{pulse-on}}$) to the disturbance period ($t_{\text{period}}$ = 200 ms) is defined as duty cycle (*DC*): $DC = t_{\text{pulse-on}}/t_{\text{period}}$. In the case of negative pulsation, *DC* is set to 10 %, resulting in air leakage during the pulse-on period of 20 ms, and thus the equivalence ratio ($\phi$) is temporally higher. While in the positive pulsation case with *DC* of 90 %, a leaner mixture is produced during the pulse-off period of 20 ms. Laser Doppler velocimetry (LDV) measurements are performed to obtain the velocity profiles of the non-reacting jet flows with negative and positive pulsations, as illustrated in Fig. 2b. The rise and fall times of the perturbed inlet velocity are about 5 ms and 2 ms, respectively.

The voltage (*V*) and current (*I*) of the MRP discharge are measured by a high-voltage probe (Tektronix P6015A) and a current monitor (Pearson 4100) and simultaneously recorded by an oscilloscope (Tektronix DPO2024B, bandwidth of 200 MHz) at a sample rate of 1 GS/s. Taking the MRP discharge sustained in the pre-mixture at $Q_{\text{air}}$ = 20 L/min and $\phi$ = 0.75 as an example, the voltage and current waveforms within the time range of 0–100 μs and the zoom-in graph within 0–2 μs are plotted in Fig. 3a and b, respectively. The peak voltage and the peak current are 7.0 kV and 22.4 A, respectively. The rise time is about 0.35 μs, and the pulse width without load is 6–8 μs [37]. After the gas breakdown, the voltage quickly falls to zero and then oscillates. The current wave shows an attenuated sinusoidal shape and then decays asymptotically to zero within 40 μs. The oscillations are expected to result from stray capacitance and inductance in the power supply, which dissipate energy in the circuit. For each pulse, the energy deposition is approximately 11.6 mJ during the breakdown process within 1 μs, corresponding to an equivalent power of 58 mW for 5 Hz MRP discharges. Compared to the estimated combustion power within the range of 0.34–1.70 kW (provided that the fuel is completely consumed), the discharge energy can be negligible.

### 2.2. Optical measurements

Fig. 1b shows a schematic of the simultaneous OH-PLIF/PIV system. In the OH-PLIF measurement, a 532 nm laser beam from a frequency-doubled Nd:YAG laser (Quanta-Ray LAB-170) pumps a dye laser (Sirah Cobra-Stretch) to generate a 283 nm laser beam with an intensity of 6 mJ/pulse. The OH-PLIF laser beam, together with a 532 nm PIV laser beam from a continuous-wave laser (MGL-W, maximum power of 18 W), is overlapped through optical lenses and transformed into a laser sheet with a thickness of 0.5 mm to illuminate the symmetry plane of the combustion zone. The fluorescence signals featuring transitions in the $A_2\Sigma^+ \leftarrow X_2\Pi$ (1,0) band of OH are detected by an intensified charge-coupled device (ICCD) camera (Princeton PI-MAX IV, 1024 × 1024 pixels) equipped with a 307 ± 10 nm optical filter. The PLIF laser is operated at a repetition rate of 5 Hz, the same as the flow pulsation.

In the PIV measurement, the flow is seeded with titanium dioxide particles with a nominal diameter of 0.5 μm, and the PIV images are recorded by a high-speed camera (Phantom v311, 1024 × 1024 pixels) at a frame rate of 4200 fps. The 30 × 30 mm field of view yields the maximum spatial resolution of 29.3 μm per pixel. Multiple passes with decreasing interrogation window size from 64 × 64 pixels to 24 × 24 pixels are performed for PIV post-processing, ensuring robustness and accuracy. For simultaneous measurements in perturbed cases, we use DG645 to synchronize the timings of the flow pulsation, PLIF, and PIV imaging.

The uncertainty of the PIV measurement due to thermophoresis is estimated by calculating the thermophoretic velocity [38]:

$$u_{TP} = -0.5\nu\frac{\nabla T}{T} \quad (2)$$

where $\nu$ is the kinematic viscosity and $T$ is the local temperature. Based on the CHEMKIN PREMIX code [39], we simulate strained premixed laminar flames of $CH_4$/air with an equivalence ratio of 0.75 and various strain rates of 110–680 $s^{-1}$ to calculate the thermophoretic velocity. The estimated uncertainty ranging from 0.5 to 0.7 cm/s can be negligible for a lean turbulent premixed flame. Additionally, the uncertainties of PIV measurements in the weakly ionized flow were discussed in the previous work [40].

Moreover, a photomultiplier tube (PMT, Hamamatsu CH-253) equipped with a 430 ± 10 nm filter is used to collect the CH* chemiluminescence. The PMT is placed far enough from the burner to ensure that the total emitted chemiluminescence can always be captured, especially under the perturbed cases where the flame oscillates up and down above the nozzle outlet. The PMT and the flow pulsation signals are synchronously recorded at a maximum sample rate of 1.25 MS/s by a multifunction data acquisition device (NI USB-6356, temporal resolution of 10 ns).

## 3. Numerical setupse

### 3.1. Turbulence and combustion modeling

In LES, the governing equations describing the conservations of mass, momentum, species, and energy are spatially filtered to remove the dependence on small-scale structures, therefore yielding the following LES equations [41]:

$$\frac{\partial\overline{\rho}}{\partial t}+\frac{\partial\overline{\rho}\widetilde{u}_j}{\partial x_j}=0 \quad (3)$$

$$\frac{\partial\overline{\rho}\widetilde{u}_i}{\partial t}+\frac{\partial\overline{\rho}\widetilde{u}_j\widetilde{u}_i}{\partial x_j}+\frac{\partial\overline{p}}{\partial x_j}=-\frac{\partial}{\partial x_j}\left[\overline{\rho}\left(\widetilde{u_iu_j}-\widetilde{u}_i\widetilde{u}_j\right)\right]+\frac{\partial\overline{\tau_{ij}}}{\partial x_j} \quad (4)$$

$$\frac{\partial\overline{\rho}\widetilde{Y}_k}{\partial t}+\frac{\partial\overline{\rho}\widetilde{u}_j\widetilde{Y}_k}{\partial x_j}=-\frac{\partial}{\partial x_j}\left[\overline{\rho}\left(\widetilde{u_iY_k}-\widetilde{u}_i\widetilde{Y}_k\right)\right]+\frac{\partial}{\partial x_j}\left(\rho D_k\widetilde{\frac{\partial Y_k}{\partial x_j}}\right)+\overline{\dot{\omega}}_k \quad (5)$$

$$\frac{\partial\overline{\rho}\widetilde{h}}{\partial t}+\frac{\partial v\widetilde{u}_j\widetilde{h}}{\partial x_j}=\frac{\partial\overline{p}}{\partial t}-\frac{\partial}{\partial x_j}\left[\overline{\rho}\left(\widetilde{u_ih}-\widetilde{u}_i\widetilde{h}\right)\right]+\frac{\partial}{\partial x_j}\left(\rho\alpha_k\widetilde{\frac{\partial h}{\partial x_j}}\right)+\overline{\dot{\omega}}_h \quad (6)$$

where the overbar "–" represents the space-filtered variable and the tilde "~" represents the density-weighted filtered variable following $\widetilde{f}=\overline{\rho f}/\overline{\rho}$, respectively. Here, $\rho$ denotes density, $t$ time, $u_i$ $i^{th}$ velocity component with $i$ = 1, 2, 3, $x_i$ $i^{th}$ Cartesian coordinate, $p$ pressure, $\tau_{ij}$ viscous stress tensor, $h$ sensible enthalpy, $Y_k$ mass fraction, $D_k$ mixture-averaged molecular diffusion coefficient, $\alpha_k$ thermal diffusion coefficient, $\dot{\omega}_k$ and $\dot{\omega}_h$ denote the source terms of $k^{th}$ species and heat from chemical reactions, respectively. The ideal gas law is applied to close the set of the governing equations, and Sutherland's law is used for modeling the laminar dynamic viscosity [41,42]. The governing equations are numerically resolved in OpenFOAM, a widely used open-source computational fluid dynamics toolbox [43].

In the above governing equations, several unclosed terms must be modeled. The popular Smagorinsky turbulence model is employed to handle the subgrid-scale (SGS) terms, including Reynolds stresses ($\widetilde{u_iu_j}-\widetilde{u}_i\widetilde{u}_j$), mass flux ($\widetilde{u_iY_k}-\widetilde{u}_i\widetilde{Y}_k$), and enthalpy flux ($\widetilde{u_ih}-\widetilde{u}_i\widetilde{h}$). Besides, the extensively validated Partially-Stirred Reactor (PaSR) subgrid combustion model, e.g., in [44], is implemented to resolve the filtered chemical reaction rate ($\overline{\dot{\omega}}_k$), which is highly nonlinear due to the exponential temperature dependence of the chemical reaction rate following the Arrhenius law. In the PaSR model, each computational cell is split into two different zones: a reacting zone and a non-reacting zone. The filtered cell reaction rate ($\overline{\dot{\omega}}_k$) is calculated by proposing a reactive volume fraction ($\gamma$):

$$\gamma=\tau_{chem}/(\tau_{chem}+\tau_{mix}) \quad (7)$$

$$\overline{\dot{\omega}}_k=\gamma\dot{\omega}_k \quad (8)$$

where $\tau_{chem}$ and $\tau_{mix}$ denote the chemical reaction time and the mixing time, respectively. The chemical reaction time can be derived from the laminar reaction rate, while the mixing time ($\tau_{mix}=C_{mix}\sqrt{\nu_t/\varepsilon}$) is determined by the turbulent kinematic viscosity ($\nu_t$) and dissipation rate ($\varepsilon$). The mixing constant ($C_{mix}$), usually ranging within 0.001–0.3 in turbulent combustion, is set to 0.1 in current cases. The skeletal reaction mechanism used for $CH_4$/air combustion is DRM-19, which is reduced from GRI-Mech 1.2 and consists of 21 species and 84 reactions [45].

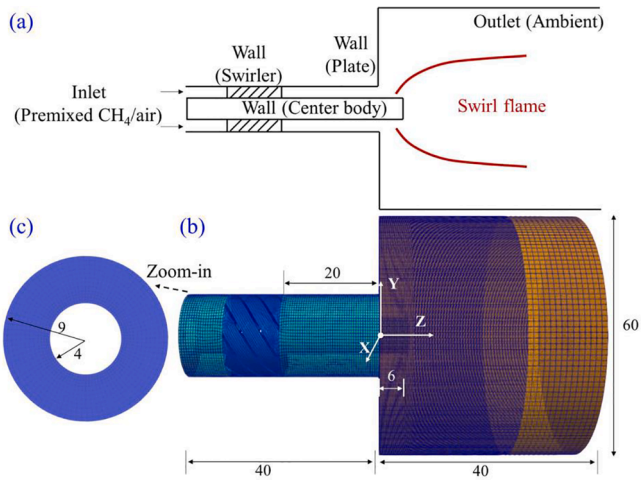


**Fig. 4.** Schematics of the (a) physical configuration, (b) computational mesh, and (c) a zoom-in view of the inlet. All dimensions are in millimeters.

**Table 1**
Settings of boundary conditions in LES.

| | Momentum | Species | Energy | Pressure |
|---|---|---|---|---|
| Inlet | Unperturbed case: $u$ = constant Perturbed case: $u = u(t)$ | Unperturbed case: $Y_{fuel}$ = constant, $Y_{air}$ = 1-$Y_{fuel}$; Perturbed case: $Y_{fuel} = Y_{fuel}(t)$, $Y_{air}$ = 1-$Y_{fuel}(t)$; | $T$ = constant | $p$ = constant |
| Outlet | $\nabla u = 0$ | $\nabla Y_k = 0$ | $\nabla T = 0$ | $p$ = constant |
| Wall | 0 | $\nabla Y_k = 0$ | $\nabla T = 0$ | $\nabla p = 0$ |

### 3.2. Physical configuration and computational setup

Fig. 4 shows the physical configuration and the computation mesh. Blocked by a bluff body, the premixed jet flow of $CH_4$ and air is injected into the ambient from an annular inlet, as depicted in the zoom-in view of Fig. 4c. As shown in Fig. 4b, the domain upstream of the nozzle outlet ($x/d_e = 0$) is constructed based on the swirl burner geometry. After a thorough domain independence study, we choose a 3D computational domain with an axial extent of 40 mm and a radial extent of 30 mm as the downstream domain in the unconfined configuration. Mesh independence is checked by testing three different meshes with 0.5, 1.1, and 1.6 million cells. Based on the tradeoff between the computation cost and numerical accuracy, a structured mesh with a total of 1.1 million cells is adopted in the present setup. The minimum grid size in reaction zones is locally refined to 0.5 mm to capture small-scale structures. The settings of boundary conditions are listed in Table 1. Here, the time-

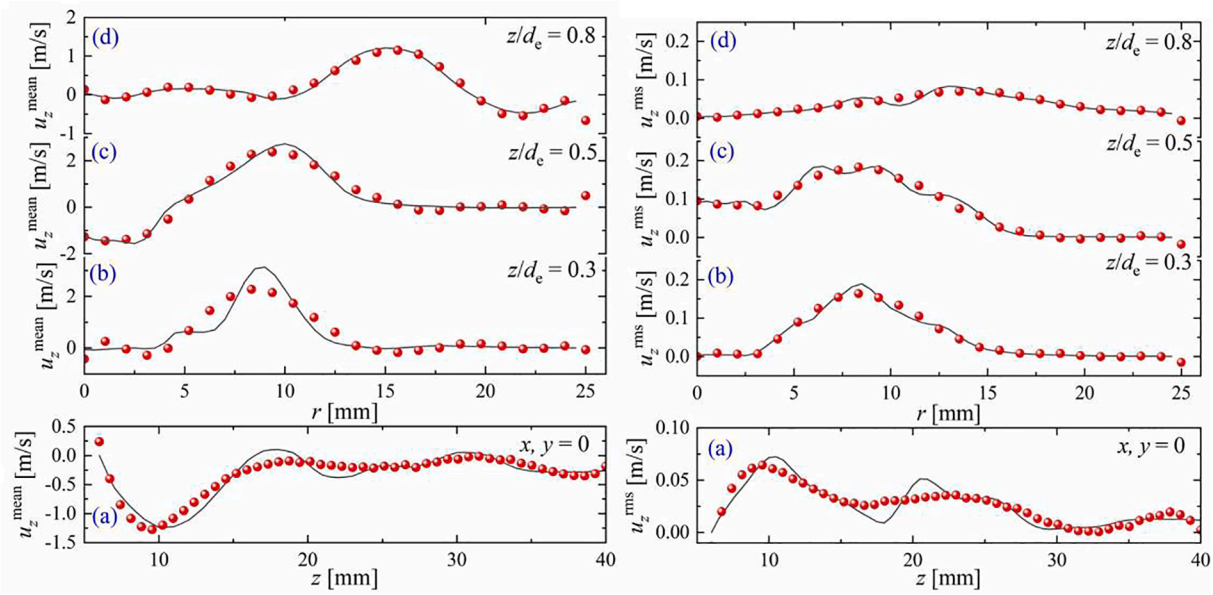


**Fig. 5.** Non-reacting swirl flows: $u_z^{mean}$ (left) and $u_z^{rms}$ (right) along (a) axial direction and (b-d) radial direction at different axial positions $z/d_e = 0.3, 0.5, 0.8$. Lines and symbols represent results from simulations and experiments, respectively.

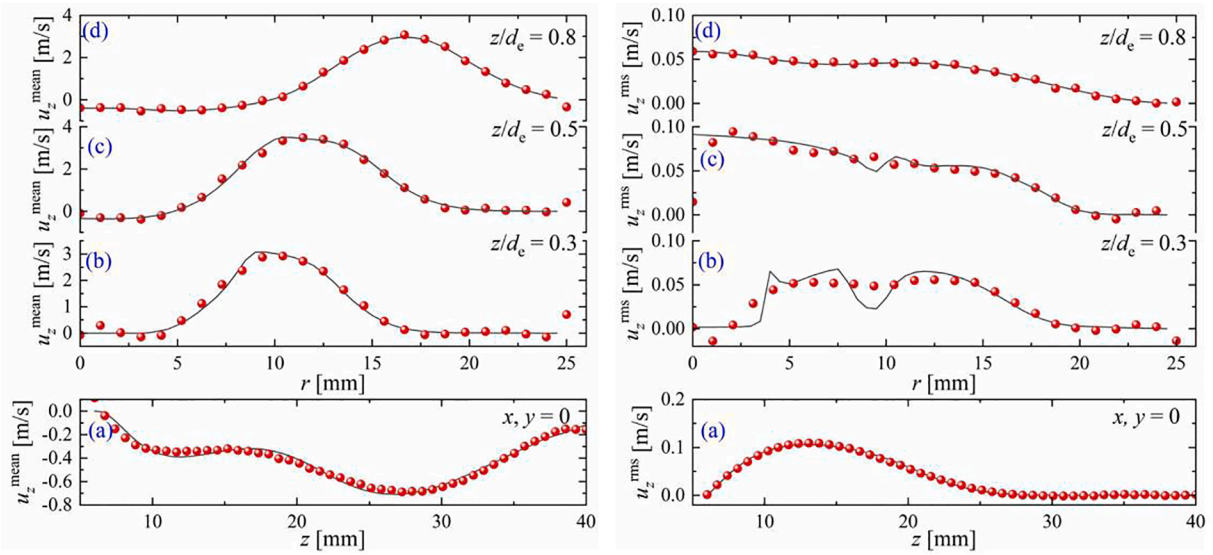


**Fig. 6.** Reacting swirl flow: $u_z^{mean}$ (left)and $u_z^{rms}$ (right) along (a) axial direction and (b-d) radial direction at different axial positions $z/d_e = 0.3, 0.5, 0.8$. Lines and symbols represent results from simulations and experiments, respectively.

dependent boundary conditions of inlet velocity and mixture components are given according to the LDV measurements (see Fig. 2b).

The Pressure-based Implicit Splitting of Operators (PISO) algorithm [46] is employed in the OpenFOAM solver to handle the pressure–velocity-density coupling. The temporal, convective, and diffusive terms are discretized using the second-order Crank Nicolson, second-order Gauss limited linear, and fourth-order Gauss cubic schemes, respectively. Good convergence is enforced by setting the maximum Courant number to 0.40, where the adaptive time step is about $1 \times 10^{-6}$ s. It takes over 6000 CPU hours on average for each case to simulate a physical time of 200 ms.

### 3.3. LES validation

To validate the LES modeling, we compare the simulated mean axial velocity ($u_z^{mean}$) and root-mean-square velocity ($u_z^{rms}$) of non-reacting and reacting swirl flows with the experimental results. Numerical and experimental velocities are obtained from 1000 PIV snapshots and 100 LES snapshots within 1 ms, respectively. For non-reacting swirl flows with $Q_{air}$ = 20 L/min, axial and radial profiles of $u_z^{mean}$ and $u_z^{rms}$ at different axial positions ($z/d_e = 0.3, 0.5, 0.8$) are shown in Fig. 5. The peak velocities at various axial positions imply that the flow spreads radially outward after leaving the burner. Negative axial velocities along the centerline (Fig. 5a and 6a) indicate the inner recirculation zone (IRZ) formed by vortex breakdown due to the bluff body [47,48]. The rms velocities near the bluff body and nozzle outlet are relatively high. Similarly, for the premixed swirl flame at $Q_{air}$ = 20 L/min and $\phi = 0.75$ in Fig. 6, the numerical velocity profiles are in reasonable agreement with the experimental results despite minor discrepancies in the rms velocities near the bluff body.

The OH contour maps superimposed with the streamlines in Fig. 7 illustrate the unperturbed flow and flame structures. The streamlines

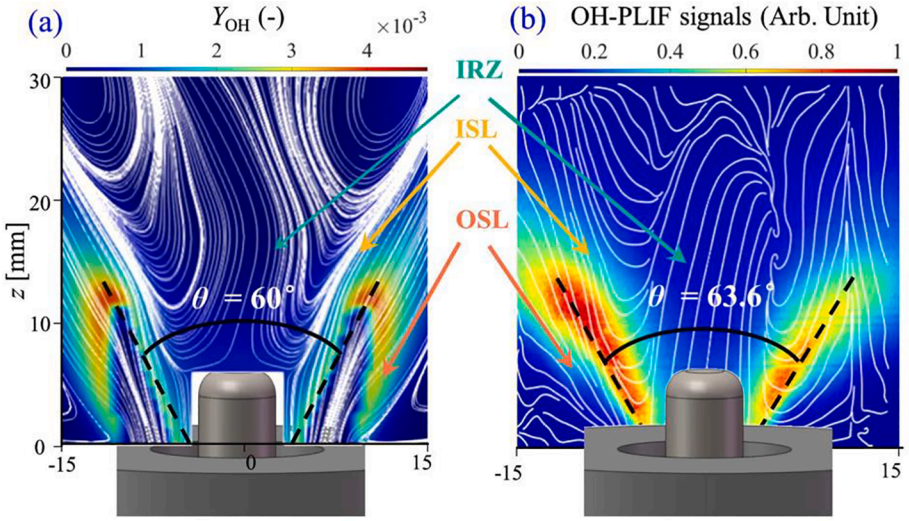


**Fig. 7.** Time-averaged OH contours superimposed with streamlines (white lines) in the symmetry plane downstream of the nozzle outlet from (a) LES and (b) simultaneous OH-PLIF/PIV results.

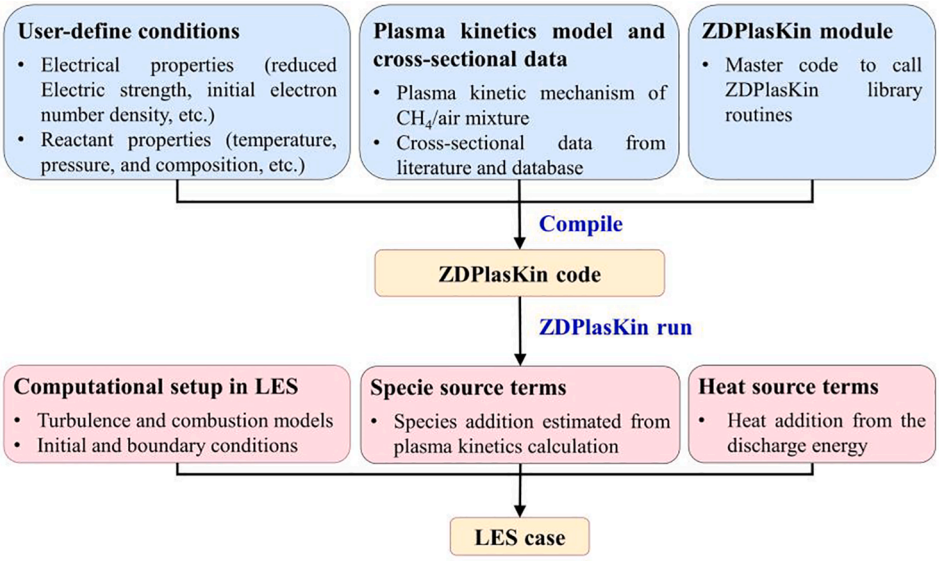


**Fig. 8.** Schematic diagram of the framework coupling the plasma kinetic model in ZDPlasKin and the chemical kinetic model in LES.

show that the annular swirling jet issuing into the ambient forms two shear layers. One is the inner shear layer (ISL) located between the jet and the IRZ, and the other is the outer shear layer (ISL) located between the jet and the outer recirculation zone (ORZ) due to the sudden expansion geometry [47]. The OH contour maps clearly show that the conically-shaped swirl flame is stabilized along the ISL. The opening angle ($\theta$) of the conical flame from LES is approximately 60 degrees, slightly smaller than the measured opening angle of 63.6 degrees. The underestimated opening angle indicates faster combustion predicted by LES, which may be attributed to the non-homogeneity assumption of PaSR. In LES, part of the flame is attached to the quartz plate due to the adiabatic setting (see Table 1). Overall, the flow and flame structures are well reproduced, which means that the LES settings employed are suitable for the current flame configuration.

### 3.4. A decoupled strategy of plasma-assisted combustion simulation

The multi-scale nature of plasma-assisted combustion significantly increases the cost and difficulty of simulation. Therefore, the current numerical studies of plasma-assisted combustion are somewhat limited to zero- and one-dimensional simulations of laminar flames [29,49], while three-dimensional simulations for plasma-assisted swirl flame are rather scarce. A skeletal mechanism called Z80 was developed to simulate microwave-assisted combustion using LES [27]. An LES case with ozone sub-mechanism was performed to isolate the effects of plasma-induced species and investigate the altered chemical kinetics [50,51]. However, few decoupled approaches in LES for plasma-assisted swirl flame have been proposed yet.

To investigate the stabilization of swirl flame by the MRP discharge, this work specifically develops a novel strategy for plasma-assisted combustion simulation, which combines ZDPlasKin for plasma kinetics calculation and LES for reactive flow modeling. The framework is shown in Fig. 8. Firstly, a validated model that integrates air plasma kinetics and the GRI-mech 3.0 mechanism is implemented to study the plasma kinetics of $CH_4$/air mixture [49]. The cross-sectional coefficients are collected from multiple databases and literature [52–54]. Based on the master library and module in ZDPlasKin, discharge conditions and the cross-sectional data are compiled into the user-defined code. Then, by

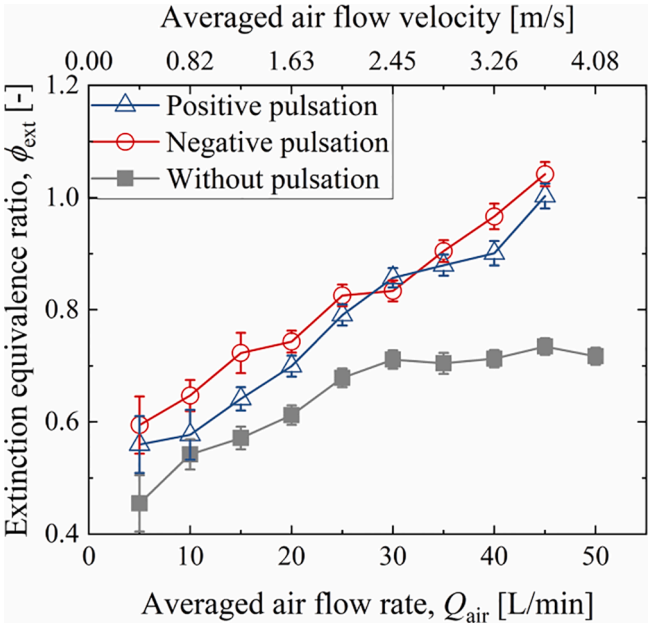


**Fig. 9.** Lean blowout limit diagram of unperturbed and perturbed flames without MRP discharge. The top and bottom axes denote averaged air flow rate and averaged air flow velocity, respectively.

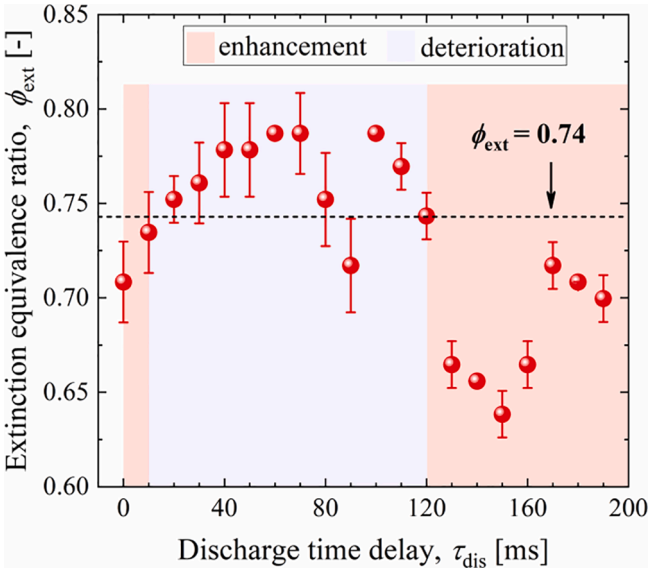


**Fig. 10.** Lean blowout limit diagram of perturbed flames with MRP discharge.

calculating electron transport and rate coefficients, ZDPlasKin resolves the discharge process and determines the concentration of the plasma-induced active species in combustion, such as atomic O, which plays an essential role in fuel oxidation and ignition. Subsequently, the output of ZDPlasKin will be adopted as specie source terms in LES simulations. Besides, the heat addition from discharge is also considered using the plasma-assisted ignition model proposed by Castela et al. [55]. Finally, LES cases with the addition of plasma-induced heat and specie source terms can be conducted to study the plasma-assisted flame dynamics. Details are available in Section 4.4. This decoupled approach not only provides a framework for 3D plasma-assisted combustion simulations of complex reactive flows, which are rather challenging in coupled codes, but also allows for detailed plasma chemistry to be considered without increasing too much computational cost.

## 4. Results and discussion

### 4.1. Stability limits

To ensure the consistency of this systematic study, we first performed illustrative experiments on the LBO limit of flames with air flow pulsation prior to the numerical analysis of flame dynamics. At atmospheric pressure (1 atm) and room temperature (298 K), the examined air flow rate ranges from 5 L/min to 50 L/min, and the corresponding air flow velocity is 0.4–4.1 m/s, yielding Reynolds number ($Re = u_{in}d_e/\nu$) of 300–2800, where $d_e$ is the equivalent hydraulic diameter. When the methane content is slowly reduced until flame extinction, the extinction equivalence ratio ($\phi_{ext}$) can be obtained as the LBO limit. Notably, in the perturbed cases with flow pulsations, $\phi_{ext}$ is determined by the time-averaged flow rate in the whole perturbed period. Through at least three repetitive operations in each case, we obtain the average as the data point of LBO limits. Uncertainties of LBO measurements, determined from standard deviations of repetitive measurements and the accuracy of the flow meters (2 %), are less than 10 % for all cases.

The LBO limits of flames without MRP discharges are shown in Fig. 9. Compared to our previous work [33], despite small differences, the trend of LBO limits with the flow rate and under various pulsations are the same. Taking a moderate flow rate of $Q_{air} = 20$ L/min as an example, the extinction equivalence ratio of PSFs without flow pulsations is 0.61. However, for PSFs under the positive and negative air flow pulsations, the extinction equivalence ratio increases to 0.70 and 0.74, i.e., 15 % and 21 %, respectively, indicating a severe deterioration of the flame stability. Moreover, at the same flow rate, $\phi_{ext}$ under negative pulsation is higher than that under positive pulsation, although the equivalence ratio of the negative pulsation case is temporally higher than the average value during the 10 % "pulse-on" period.

Furthermore, the effects of MRP discharges on perturbed flames are investigated under various flow rates. The frequency of the plasma discharge is set to 5 Hz, which is consistent with that of the flow pulsation. The discharge time delay ($\tau_{dis}$) between the pulsed discharge and the flow pulsation in each cycle ranges from 0 ms to 200 ms. As shown in Fig. 10, for the flame with $\phi_{ext} = 0.74$, when $\tau_{dis}$ ranges from 30–130 ms, $\phi_{ext}$ does not decrease and even slightly increases. Prior literature reported that in the pulsed discharge, the shock wave is generated due to ultrafast heating and the corresponding hydrodynamic effect increases the wrinkling of the flame front [26,56]. The hydrodynamics of plasma-induced shockwave and flow pulsation may be responsible for the accelerated flame extinction [33]. However, when $\tau_{dis}$ is within 0–20 ms or 130–200 ms, a lower $\phi_{ext}$ of 0.64 can be achieved, indicating the enhanced flame stability by plasma discharge. Specifically, the LBO limit is extended by up to 14 % at $\tau_{dis} = 150$ ms by applying the 5 Hz plasma discharge. Although the present experiments are mainly carried out with laminar swirl flames, the extension effect of the MRP discharge on LBO limits can be improved by increasing the repetition rate [33]. Our previous work [30] also demonstrated that high-frequency gliding arc discharge driven by ~7.5 kHz alternating-current power can stabilize turbulent swirl flames with higher flow rates under air flow pulsations. Next, the deteriorated flame stability under air flow pulsation and plasma-assisted stabilization will be intensively studied.

### 4.2. Visualization of flame extinction under air flow pulsations

Fig. 11 shows the time-sequential OH-PLIF contours with superimposed velocity vectors to visualize the flame extinction under low-frequency flow pulsations. According to the evolution of the high-intensity OH zones, the flame response to negative pulsation can be roughly divided into two stages: (i) the OH intensity is firstly enhanced within 0–30 ms; (ii) then it is weakened and eventually almost extinguished. Meanwhile, the overall flow field is disturbed due to the flow pulsation. When the flame is enhanced, the IRZ is slightly widened. We further quantitively study the flow non-equilibrium process from the

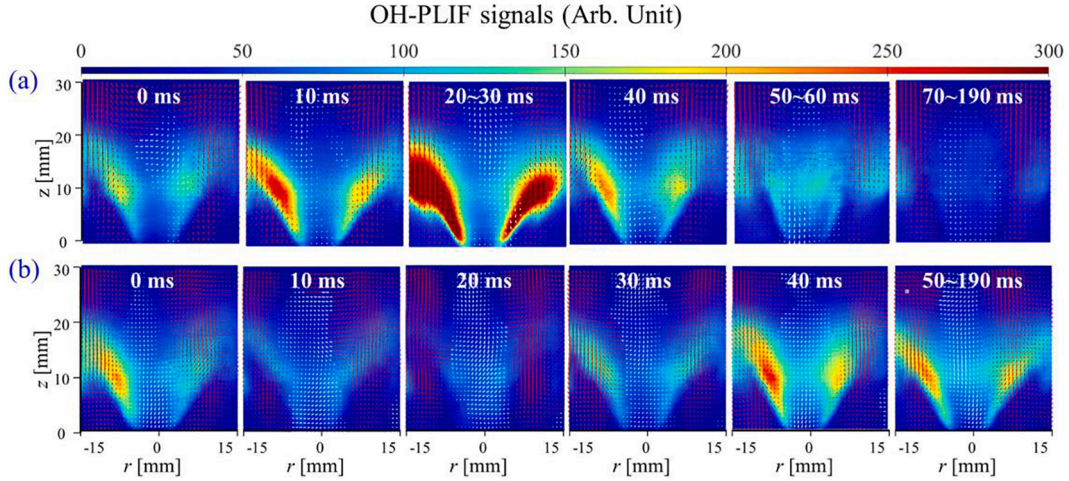


**Fig. 11.** Sequential OH-PLIF images of flames under (a) negative and (b) positive flow pulsations. Vector plots are superimposed where negative axial velocities are displayed in white. The timing denotes the time delay between the triggering of pulsed flow disturbance and the ICCD camera.

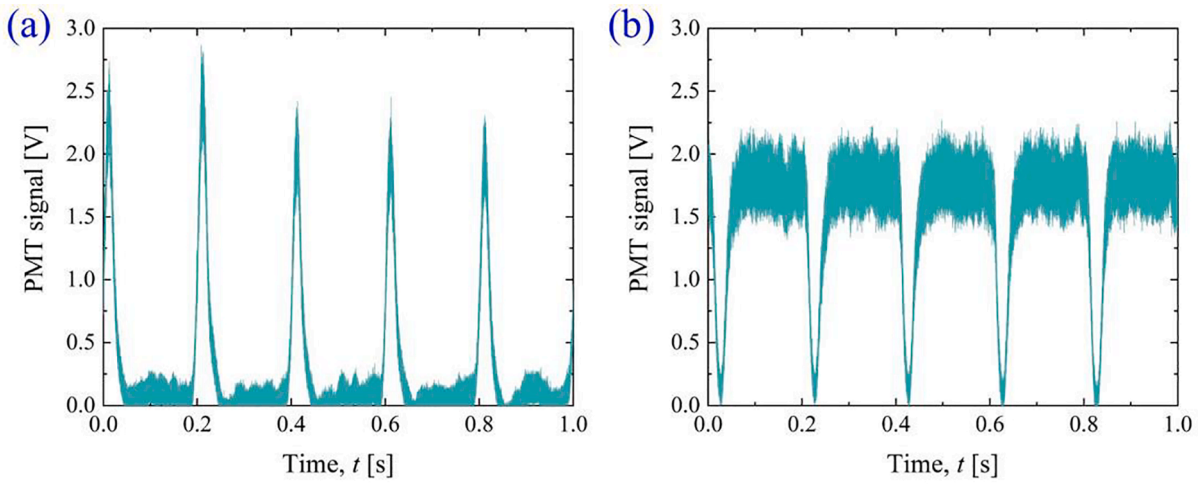


**Fig. 12.** PMT signals of flames under (a) negative and (b) positive flow pulsations.

numerical velocity profiles. Regarding the dynamic response of flame to the positive pulsation, the trend is opposite: (i) the OH intensity is weakened within 0–40 ms, indicating a weaker flame; (ii) subsequently, the weak flame is reignited and eventually sustained over the rest of the disturbance cycle. This reignition phenomenon can be used to explain the higher extinction equivalence ratio under positive pulsation. Obviously, the flame extinction and reignition should be attributed to not only the variation of the leaner equivalence ratio but also the changed flow field caused by the low-frequency, high-amplitude flow pulsation. Flame responses are quantitatively discussed in Section 4.3.

The global heat release rate measurements are also good indicators for the flame extinction and reignition. After subtracting the background noise of 0.3 V, the PMT signals of PSFs under both negative and positive pulsations are depicted in Fig. 12. Generally, the time-dependent PMT signals are consistent with the OH-PLIF observations. In the post-pulsation stage, we can clearly observe the extinction for negative pulsation and the reignition for positive pulsation, respectively. Hence, from the results of the sequential OH-PLIF images and the PMT signals, it can be elucidated that under the same averaged flow rate, the deterioration effects of the negative flow pulsations on the PSFs are more significant.

Numerical analysis of flame dynamics under air flow pulsations.

A quantitative LES analysis is further performed to reveal the dynamics of perturbed flames. Note that, we employ time-varying boundary conditions of inlet velocity and equivalence ratio in LES according to the LDV-calibrated flow pulsations (see Fig. 2). For negative and positive cases, the time-averaged air flow rates are 20 L/min and the time-averaged equivalence ratios are 0.75.

To obtain a comprehensive insight into the unsteady extinction process, both the flow- and the chemical-nonequilibrium processes under flow pulsations should be analyzed. Flame stretch rate ($\kappa$), the inverse of which is a good representation of the characteristic flow time ($\tau_{\text{flow}}$) [57], is utilized to interpret the sudden change in the flow field caused by flow pulsations. It can be calculated from the following formula [41]:

$$\kappa = \kappa_s + \kappa_{\text{curv}} = -n_i n_j \frac{\partial u_i}{\partial x_j} + \frac{\partial u_i}{\partial x_i} - s_L \frac{\partial n_i}{\partial x_i} \tag{9}$$

where $\kappa_s$ is the hydrodynamic strain rate, and $\kappa_{\text{curv}}$ is the flame curvature, $s_L$ is the flame speed. In a weakly wrinkled flame, the flame curvature is much smaller than the hydrodynamics strain rate, allowing us to ignore the flame curvature term when evaluating the flame stretch rate [58]. The hydrodynamic strain rate term can be readily calculated from the numerical three-dimensional velocity profiles. In addition to the flame stretch rate, the extensively used parameter, volumetric heat release rate ($\dot{q}_c$), is extracted to illustrate the chemistry-nonequilibrium

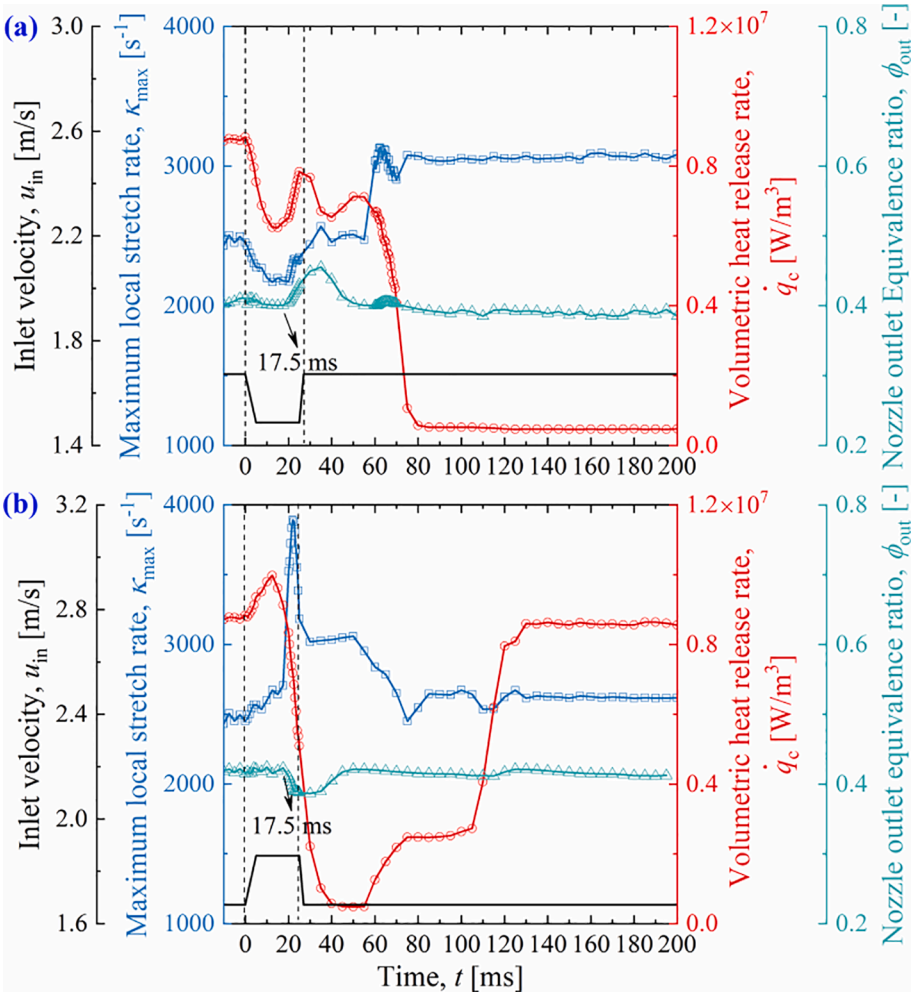


**Fig. 13.** Variations of the inlet velocity, equivalence ratio at nozzle outlet, maximum local stretch rate, and volumetric heat release rate of flames under (a) the negative and (b) positive pulsations.

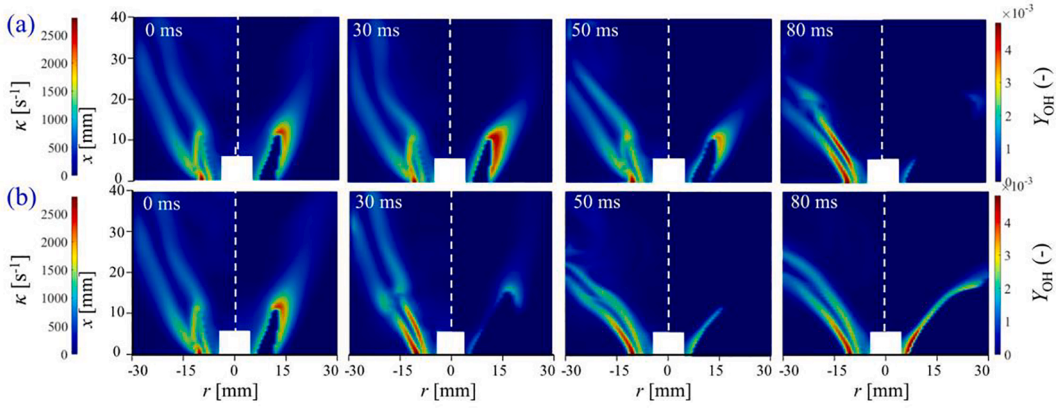


**Fig. 14.** Combined contour maps of the local stretch rate (left) and OH concentration (right) of flames at different moments under (a) negative and (b) positive flow pulsations.

process. Besides, the local equivalence ratio is also essential to flame blowout, which directly affects the chemical reaction rates and the flame speed [59]. In premixed combustion, the equivalence ratio at the nozzle outlet ($\phi_{out}$) is suitable for describing the pre-mixture entering the combustion zone.

Fig. 13 shows a combined plot of equivalence ratio at nozzle outlet ($\phi_{out}$), maximum local stretch rates ($\kappa_{max}$), and volumetric heat release rate, with the inlet velocity ($u_{in}$) as a reference for transient operation. Fig. 14 shows the contour maps of the local stretch rate and OH mass fraction. When applying the negative pulsation, $\phi_{out}$ first increases and then returns to the initial value until the next disturbance cycle. However, the responses of $\dot{q}_c$ and $\kappa_{max}$ are much more complicated. Firstly, $\dot{q}_c$ and $\kappa_{max}$ decrease simultaneously with $u_{in}$ at $t = 0$ ms. Subsequently, $\kappa_{max}$ and $\dot{q}_c$ recover at $t = 20$ ms and fluctuates within 20–60 ms. In fact,

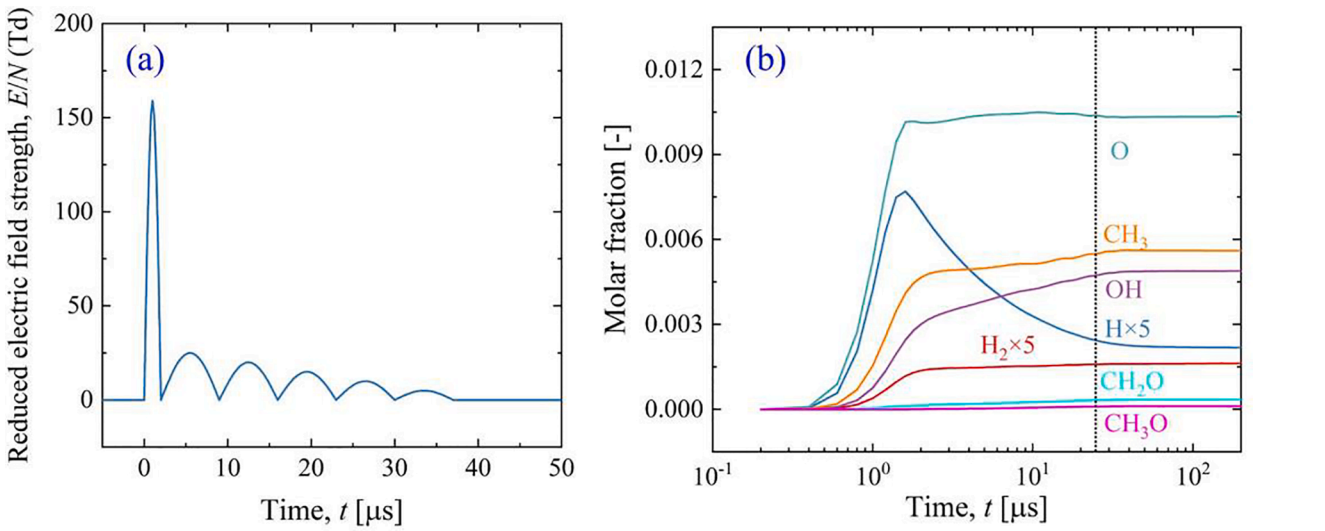


**Fig. 15.** (a) The initial conditions and (b) the calculated molar fractions of the plasma-induced radicals in ZDPlasKin. A vertical dotted line in Fig. 15b indicates the end of the discharge.

The OH contour at 30 ms presents the slightly enhanced combustion due to the increased $\phi_{out}$. However, after $t$ = 60 ms, $\kappa_{max}$ increases and reaches a plateau of ~3200 $s^{-1}$ much higher than the initial level of ~2400 $s^{-1}$, while $\dot{q}_c$ drops dramatically to zero at around $t$ = 80 ms, at this moment the flame is locally extinguished (see Fig. 14a). Contours in Fig. 14 also show that the high strain rate mainly distributes in ISL and along the flame boundary, and the global blowout eventually occurs at $t$ = 80 ms. It suggests that the flow pulsation results in a higher stretch rate through the intense velocity gradient, and thus leads to a greater likelihood of flame extinction. The nonlinear response, especially the continuous increment of the local stretch rate during the post-pulse stage of the negative flow pulsation, should be attributed to the movement of the perturbed flame [60]. Moreover, it can be deduced that the combination of time-dependent variations of the maximum local stretch rate and heat release rate is a good marker of flame extinction and reignition.

Moreover, there is a time delay of 17.5 ms between the turning points of the local stretch rate/volumetric heat release rate and the equivalence ratio. Here, we define a convective time ($\tau_{conv}$) as the time required for the pre-mixture to propagate from the nozzle inlet ($x/d_e = -2$) to outlet ($x/d_e = 0$). It can be calculated by the following formula:

$$\tau_{conv} = \int_0^L (1/u_z)\, dz \tag{10}$$

where $u_z$ is the local axial velocity and $L$ is the axial distance between the nozzle inlet and outlet. The convective time of 18.0 ms is close to the time delay of 17.5 ms. It indicates that the convection process is the main cause of the time delay between the local stretch rate/volumetric heat release rate and the equivalence ratio upstream of the flame root.

The flame response under positive pulsation is significantly different. As seen in Fig. 13b, first, $\kappa_{max}$ significantly increases and $\dot{q}_c$ decreases. The OH contour in Fig. 14b also indicates that the flame is locally extinguished. However, at the post-pulse stage, the equivalence ratio recovers to an initially high level. The sufficient fuel supply before a complete flame quenching leads to second turning points of elevated $\kappa_{max}$ and decreasing $\dot{q}_c$. Consequently, the flame reignition is observed at $t$ = 80 ms. The reignition phenomena can explain the discernible difference between the LBO limits under the negative and positive flow pulsations, which is also validated by the sequential OH-PLIF images in Fig. 11.

### 4.3. Plasma-assisted stabilization under air flow pulsations

As described in Section 3.4, we attempt to incorporate the plasma effects to interpret the role of the MRP discharge in the weak flame. To account for the thermal effect, a heat source term is modeled according to a model for plasma-assisted ignition [55]. It was reported that when the reduced electric field ($E/N$) is within 100–400 Td, approximately 90 % of the total discharge energy goes into the population of vibrational (35 %) and electronic (55 %) of $N_2$ molecules, which is eventually used for specie dissociation (mainly atomic oxygen) and gas heating [55,61]. In this case, $E/N$ mainly ranges from 0 to 160 Td, and the fraction of the discharge energy deposition used for ultrafast gas heating can be roughly estimated to be 20 % [61]. Regarding the kinetic effects, by resolving the plasma kinetics in the reactive flow, concentrations of plasma-induced radicals from ZDPlasKin outputs can be retrieved as the source terms in LES. When the flame is nearly distinguished, the fresh unburnt mixture of methane and air is intensively entrained in the inner recirculation zone. In addition, preliminary tests confirmed that the hot products of $H_2O$ and $CO_2$ have minor impacts on the ZDPlasKin output. Therefore, at this moment, this work calculates the plasma chemistry in a mixture of methane and air.

The reduced electric field strength ($E/N$) is estimated from the measured voltage and simplified to a damped sinusoidal waveform, as shown in Fig. 15a. Taking the typical case of $T$ = 1500 K and $\phi$ = 0.75 as an example, simulated concentrations of the main active radicals are shown in Fig. 15b. During discharge, the mole fractions of active radicals increase through the dominating electron impact reactions. After then, the radical production and consumption reach a balance due to decay and recombination between the excited species and positive ions [49]. The oscillation of $E/N$ after breakdown has relatively little impact on the species concentrations. Since the species concentrations quickly accumulate and saturate within several microseconds and the time step in LES is in the order of 1 μs, the saturated concentrations can be reasonably supplied into the LES simulation.

### 4.4. Plasma-induced species modeling

The plasma-induced source terms depend on the local temperature and mixture composition, which are time-varying and spatially non-uniform. However, due to the limitation of ZDPlasKin as a zero-dimensional computation and the lack of interface between ZDPlasKin and LES, the ZDPlasKin output and the corresponding LES source terms cannot be directly updated in real-time. Therefore, we first implement

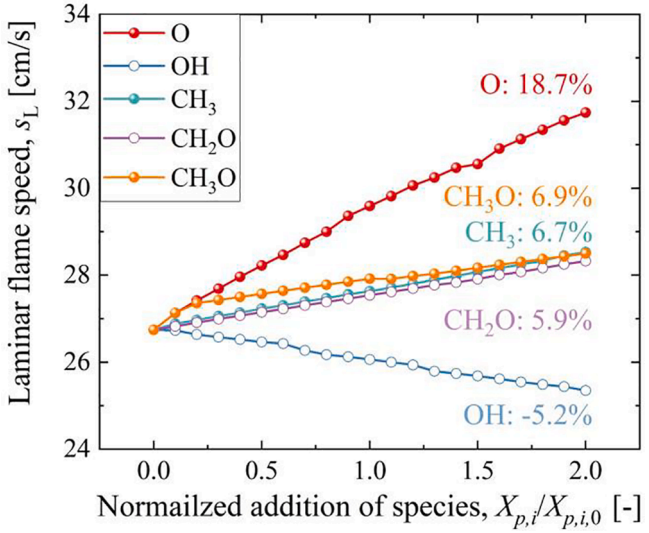


**Fig. 16.** Dependence of laminar flame speed on the species addition. The maximum changes of flame speed are marked.

**Table 2**
A list of the fitting coefficients and determination of coefficients.

| | $a$ [-] | $b$ [$K^{-1}$] | $C$ [-] | $d$ [$K^{-1}$] | $R^2$ |
|---|---|---|---|---|---|
| O | $1.71 \times 10^{-2}$ | $7.31 \times 10^{-8}$ | $-8.45 \times 10^{-3}$ | $-3.69 \times 10^{-7}$ | 0.9922 |
| OH | $4.04 \times 10^{-3}$ | $-6.18 \times 10^{-7}$ | $9.18 \times 10^{-4}$ | $8.59 \times 10^{-7}$ | 0.9053 |
| $CH_3$ | $8.86 \times 10^{-4}$ | $-5.28 \times 10^{-7}$ | $6.06 \times 10^{-3}$ | $7.59 \times 10^{-7}$ | 0.9991 |
| $CH_2O$ | $5.92 \times 10^{-4}$ | $-9.23 \times 10^{-8}$ | $-3.83 \times 10^{-4}$ | $1.63 \times 10^{-7}$ | 0.9977 |
| $CH_3O$ | $6.19 \times 10^{-5}$ | $9.95 \times 10^{-8}$ | $-2.60 \times 10^{-4}$ | $9.26 \times 10^{-8}$ | 0.9995 |

various initial conditions to obtain a collection of ZDPlasKin outputs. Subsequently, the relationship between ZDPlasKin outputs and independent variables ($T$ and $\phi$) is established as $X_{p,i}(T, \phi)$. $X_{p,i}$ denotes the molar fraction of the $i^{th}$ plasma-induced species. The plasma-induced source terms can be modeled at each LES timestep, avoiding computationally expensive iterations between the ZDPlasKin and LES. In this way, decoupling between ZDPlasKin and LES can be achieved.

We first conduct a sensitivity analysis on all species in the DRM-19 mechanism to determine which ones are critical to the combustion. The main target during the analysis is the laminar flame speed ($s_L$) at conditions of 1 atm and 300 K. The dependence of the laminar flame speed on the species addition are shown in Fig. 16. Note that for each species, $X_{p,i}$ varies from 0 % up to 200 % of a reference value $X_{p,i,0}$, subtracted from a typical ZDPlasKin output ($T = 1500$ K and $\phi = 0.75$). Here, we just show the species that results in over ± 5 % modification in laminar flame speed, i.e., O, OH, $CH_3$, $CH_2O$, and $CH_3O$ radicals. Note that, the decrement of the laminar flame speed under OH addition should be attributed to the change in net reaction rate of $H + O_2 \rightarrow H + OH$, which is the most influential reaction of laminar flame speed. It can be also seen from Fig. 15b that molar fractions of these radicals are relatively high, especially the O atom. It is mainly due to the electron impact dissociation of $O_2$ (e.g., $O_2 + e \rightarrow O + O + e$), collisions of electronically excited nitrogen with $O_2$ (e.g., $N_2(A^3\Sigma) + O_2 \rightarrow N_2(X^1\Sigma) + O + O$), and recombination of electron and positive ions (e.g. $e + O_2^+ \rightarrow O + O$) [49,62]. Some studies also reported that the dominant active specie in plasma discharge is atomic oxygen, which initiates and accelerates the chain-branching reactions, thus plays a critical role in the kinetic enhancement [62]. $CH_3$, $CH_2O$, and $CH_3O$ were identified as key species in $CH_4$/air flames [63]. Conclusively, these main active radicals produced through plasma kinetics should be considered in the LES simulation.

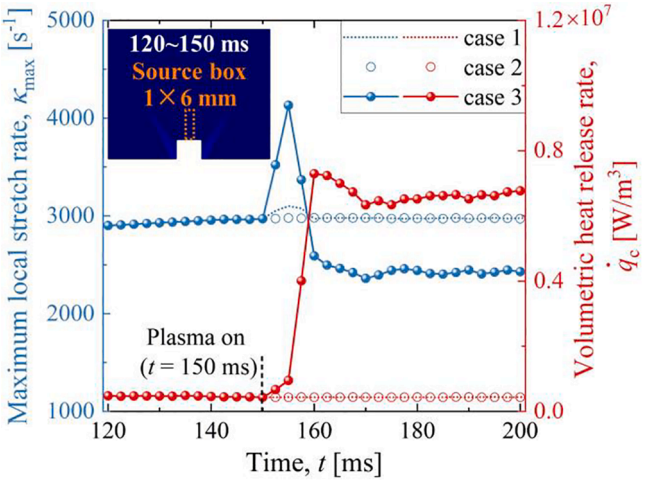


**Fig. 17.** Variations of the maximum local stretch rate and heat release rate in cases 1, 2, and 3.

Then, we test a case matrix consisting of two independent variables ($T$ and $\phi$) in ZDPlasKin, where $T$ ranges from 1000 K to 3000 K with an interval of 100 K and $\phi$ ranges from 0.6 to 1.0 with an interval of 0.05. Subsequently, we adopt the following formula as the fitting function of the simulated results (see the contours in Appendix):

$$X_{p,i}(T, \phi) = a_i + b_i \times T + c_i \times \phi + d_i \times \phi \times T \quad (12)$$

where $a$, $b$, $c$, and $d$ denote the fitting coefficients, subscript $i$ is the index of the species. The determination of coefficient $R^2$ close to 1 indicates a satisfying fitting. All the fitting coefficients are listed in Table 2. Conclusively, the relationship between the plasma-induced species and the local temperature and reactant is established.

### 4.5. Numerical analysis in plasma-assisted combustion

In LES case, taking the following case as an example: the flame is extinguished early at $t = 60$ ms under negative flow pulsations, then the MRP discharge is numerically applied at $t = 150$ ms, the moment when the plasma enhancement effects are distinguished (see Section 4.1). Then, we set up a cylindrical topological structure with a size of $D \times H = 1 \times 6$ mm as the source region (see the inner graph of Fig. 17), which is estimated from the emission image of the MRP discharge. Three cases are simulated: (1) adding only the heat source term; (2) adding only the specie source term; (3) adding both the heat and specie source terms.

Fig. 17 shows variations of the maximum local stretch rate and heat release rate in cases 1, 2, and 3. Overall, the addition of plasma-induced heat or radicals alone in case 1 and case 2 hardly affects the flame extinction, while case 3 observes the flame reignition (see Fig. 18). Here, it must be addressed that there are two key requirements for ignition: one is high temperature to initiate the chain-branching reactions and the other is the radical production chain-branching reactions faster than the chain-termination reactions [20]. It can be deduced from the numerical results that adding heat (case 1) or radical (case 2) alone cannot meet the requirement of ignition of the unburnt reactant, making little difference on the chain chemical reactions. Therefore, when turning the plasma on, the volumetric heat release rate and the stretch rate are seldom influenced, indicating a failure of flame reignition. Besides, the small increment of local stretch rate in case 1 can be explained by the altered local gas density and velocity due to the heat addition.

In case 3, as soon as the plasma is activated at $t = 150$ ms, the heat release rate is exponentially increased. Apparently, it results from

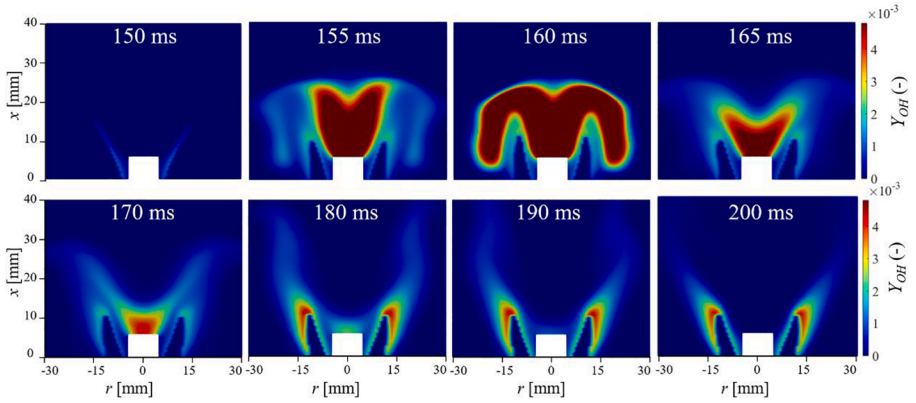


**Fig. 18.** Sequential OH contour maps of the flame under negative air flow pulsation for case 3.

ignition, which is an exothermic, chain-branching reaction process for fuel oxidation. Meanwhile, the maximum local stretch rate decreases from 3000 $s^{-1}$ to 2500 $s^{-1}$, close to the value of unperturbed flames. It indicates that in the reignited reaction zone, the local temperature rise caused by the enhanced chemical reactions smooths the velocity gradient. The reignition phenomenon of perturbed PSF with the assistance of the MRP discharge is well predicted by the simulation. Furthermore, it can be concluded from the comparative simulations that the thermal and kinetic effects of the MRP discharge play indispensable roles in improving flame stabilization.

On the one hand, the energy supply from plasma leads to a significant temperature increase, for example, the local temperature exceeds 2400 K at the onset of plasma activation. Following the exponential temperature dependence in Arrhenius's law, the chemical reactions are dramatically accelerated and the chain-branching process is initiated. On the other hand, plasma-induced additives produce heat from the accelerated chain branching reactions, such as $O + H_2 \rightarrow H + OH$, to enhance the thermal effect [20]. Conclusively, the thermal and kinetic

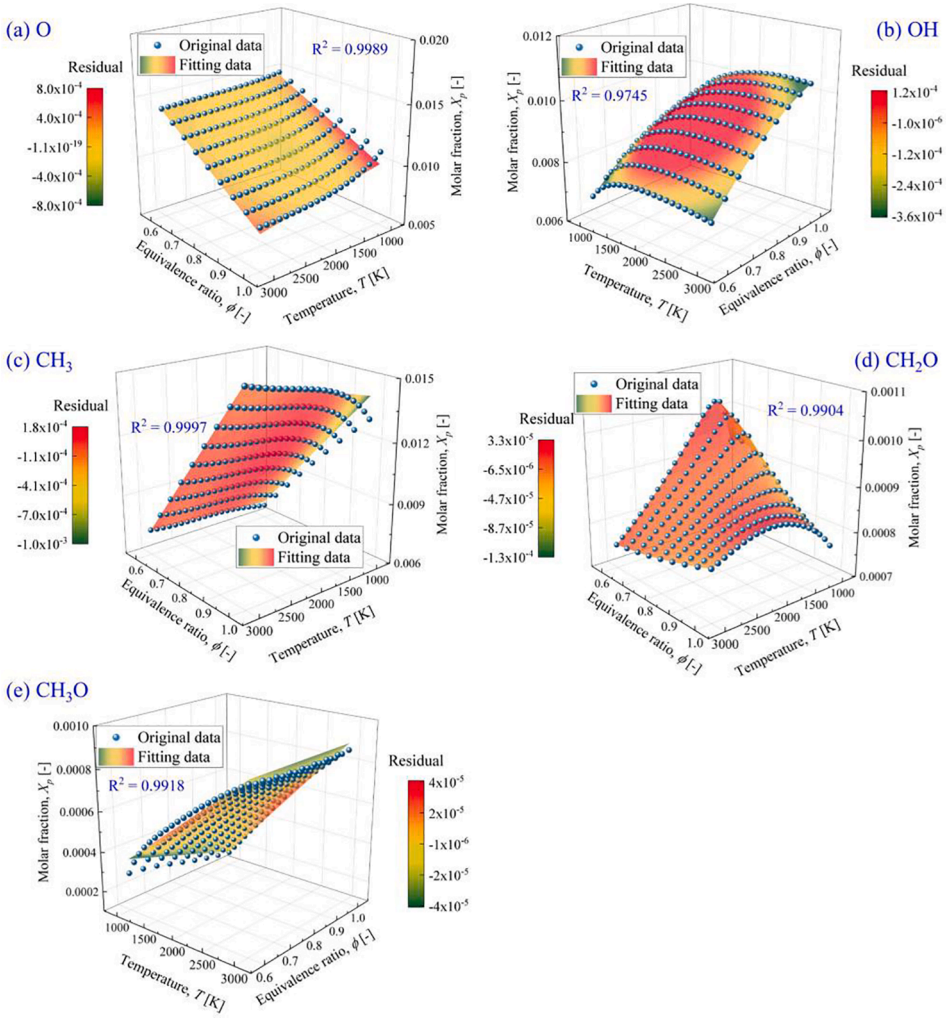


**Fig. A1.** Molar fractions of (a) O, (b) OH, (c) $CH_3$, (d) $CH_2O$, and (e) $CH_3O$ radicals produced in plasma kinetic processes.

effects of the MRP discharge work in a synergistic manner, fulfilling the two key requirements for ignition and ultimately leading to flame reignition. More importantly, it also shows that the current design of the MRP discharge with combined thermal-kinetic enhancement pathways is suitable for flame stabilization.

## 5. Conclusion

This study systematically investigates the effects of low-frequency flow pulsations and microsecond repetitively pulsed discharges on flame extinction and stabilization characteristics. As reported in the previous work [33], in the absence of plasma discharge, the negative and positive flow pulsations significantly deteriorate the LBO limit of PSF by 21 % and 15 %, respectively.

In this work, the validated LES simulation and simultaneous OH-PLIF/PIV measurement are performed to identify swirl flame structures and resolve dynamic flame evolution. In the presence of air flow pulsation, excessive stretch rates (~33 % increment) due to the abrupt change in flow structures are revealed, causing the local flame extinction in the inner shear layer. Meanwhile, the relationship between the maximum local flame stretch rate, the maximum local heat release rate, and the local equivalence ratio is established to quantitatively analyze the unsteady flame extinction under air flow pulsations. When the increment of the local stretch rate and the decrement of the heat release rate are in phase, extinction of perturbed flames is observed. Otherwise, the flame will be reignited. The intrinsic convective time delay between the variations of the stretch rate/heat release rate and equivalence ratio is divulged, which is determined by the convective process of the flow pulsation in the pipeline. Further, it is concluded that the combination of time-dependent variations of the maximum local stretch rate and volumetric heat release rate can be used as a good indicator of flame extinction.

Implementing plasma discharge can extend the LBO limit by up to 14 % at the discharge time delay within 0–20 ms and 130–200 ms. The second contribution of this work is the development of a decoupled simulation approach for the discharge and combustion processes to investigate the underlying mechanism of plasma-assisted stabilization. This approach integrates the plasma chemistry derived from ZDPlaskin and plasma-induced heat source term into the LES simulation to address the kinetic and thermal effects, respectively. It not only significantly simplifies the simulation of the plasma-assisted combustion (in terms of the computational cost), but also incorporates plasma effects rationally and comprehensively. Through the comparative cases, the numerical study well predicts the plasma-assisted reignition phenomenon of perturbed PSF, further demonstrating the indispensability of the thermal and kinetic effects of the MRP discharge in improving flame stability.

## CRediT authorship contribution statement

**Jinguo Sun:** Conceptualization, Methodology, Investigation, Data curation, Writing – original draft. **Wei Cui:** Conceptualization, Methodology. **Yong Tang:** Methodology, Writing – review & editing. **Chendong Kong:** Methodology, Writing – review & editing. **Shuiqing Li:** Supervision, Writing – review & editing, Funding acquisition.

## Declaration of Competing Interest

The authors declare that they have no known competing financial interests or personal relationships that could have appeared to influence the work reported in this paper.

## Data availability

We would like to share some data in some cases and when needed.

## Acknowledgments

This work is funded by the National Natural Science Foundation of China (Grants numbers. 91641204 and 51725601).

## Appendix

Fig. A1 shows the molar fractions of (a) O, (b) OH, (c) $CH_3$, (d) $CH_2O$, and (e) $CH_3O$ radicals produced in plasma kinetic processes. Original data and the fitting data are represented by the points and contour surface. Contours are colored by fitting residuals.

## References

[1] Lieuwen TC, Yang V. Combustion instabilities in gas turbine engines: operational experience, fundamental mechanisms, and modeling. American Institute of Aeronautics and Astronautics; 2005.
[2] Matalon M. Intrinsic flame instabilities in premixed and nonpremixed combustion. Annu Rev Fluid Mech 2007;39:163–91. https://doi.org/10.1146/annurev.fluid.38.050304.092153.
[3] Huang Y, Yang V. Dynamics and stability of lean-premixed swirl-stabilized combustion. Prog Energy Combust Sci 2009;354:293–364. https://doi.org/10.1016/j.pecs.2009.01.002.
[4] Poinsot T. Prediction and control of combustion instabilities in real engines. Proc Combust Inst 2017;361:1–28. https://doi.org/10.1016/j.proci.2016.05.007.
[5] McManus KR, Poinsot T, Candel SM. A review of active control of combustion instabilities. Prog Energy Combust Sci 1993;191:1–29. https://doi.org/10.1016/0360-1285(93)90020-F.
[6] Nair S, Lieuwen T. Acoustic detection of blowout in premixed flames. J Propul Power 2005;211:32–9. https://doi.org/10.2514/1.5658.
[7] Mongia HC, Held TJ, Hsiao GC, Pandalai RP. Challenges and progress in controlling dynamics in gas turbine combustors. J Propul Power 2003;195:822–9. https://doi.org/10.2514/2.6197.
[8] Rayleigh L. The explanation of certain acoustical phenomena. Nature 1878;18455:319–21. https://doi.org/10.1038/018319a0.
[9] Tao C, Zhou H. Effects of superheated steam on combustion instability and NOx emissions in a model lean premixed gas turbine combustor. Fuel 2021;288:119646. https://doi.org/10.1016/j.fuel.2020.119646.
[10] Zhou H, Tao C. Effects of annular N2/O2 and CO2/O2 jets on combustion instabilities and NOx emissions in lean-premixed methane flames. Fuel 2020;263:116709. https://doi.org/10.1016/j.fuel.2019.116709.
[11] O'Connor J, Acharya V, Lieuwen T. Transverse combustion instabilities: acoustic, fluid mechanic, and flame processes. Prog Energy Combust Sci 2015;49:1–39. https://doi.org/10.1016/j.pecs.2015.01.001.
[12] Rosfjord TJ, Cohen JM. Evaluation of the transient operation of advanced gas turbine combustors. J Propul Power 1995;113:497–504. https://doi.org/10.2514/3.23870.
[13] Culick FE, Kuentzmann P. Unsteady motions in combustion chambers for propulsion systems. NATO Research and Technology Organization Neuilly-Sur-Seine (France); 2006.
[14] Palies P. Stabilization and dynamic of premixed swirling flames: prevaporized. Stratified: Partially, and Fully Premixed Regimes. Elsevier Science; 2020.
[15] Kharoufah H, Murray J, Baxter G, Wild G. A review of human factors causations in commercial air transport accidents and incidents: From to 2000–2016. Prog Aeosp Sci 2018;99:1–13. https://doi.org/10.1016/j.paerosci.2018.03.002.
[16] Cohen J, Bennett JJ. An experimental study of the transient flow over a backward-facing step. 34th Aerospace Sciences Meeting and Exhibit 1996; American Institute of Aeronautics and Astronautics. https://doi.org/10.2514/6.1996-322.
[17] Richards GA, Straub DL, Robey EH. Passive control of combustion dynamics in stationary gas turbines. J Propul Power 2003;195:795–810. https://doi.org/10.2514/2.6195.
[18] Candel S. Combustion dynamics and control: Progress and challenges. Proc Combust Inst 2002;291:1–28. https://doi.org/10.1016/S1540-7489(02)80007-4.
[19] Ju RY, Wang JH, Xia H, Li YM, Mu HB, Zhang GJ, et al. Effect of rotating gliding arc plasma on lean blow-off limit and flame structure of bluff body and swirl-stabilized premixed flames. IEEE Trans Plasma Sci 2021;4911:3554–65. https://doi.org/10.1109/TPS.2021.3121286.
[20] Ju Y, Sun W. Plasma assisted combustion: dynamics and chemistry. Prog Energy Combust Sci 2015;48:21–83. https://doi.org/10.1016/j.pecs.2014.12.002.
[21] Ju YG, Lefkowitz JK, Reuter CB, Won SH, Yang XL, Yang S, et al. Plasma assisted low temperature combustion. Plasma Chem Plasma Process 2016;361:85–105. https://doi.org/10.1007/s11090-015-9657-2.
[22] Huang S, Wu Y, Zhang K, Sun J, Jin D, Li Y. Experimental investigation on spray and ignition characteristics of plasma actuated bluff body flameholder. Fuel 2022;309:122215. https://doi.org/10.1016/j.fuel.2021.122215.
[23] Lin B, Wu Y, Zhu Y, Song F, Bian D. Experimental investigation of gliding arc plasma fuel injector for ignition and extinction performance improvement. Appl Energy 2019;235:1017–26. https://doi.org/10.1016/j.apenergy.2018.11.026.
[24] Starikovskiy A, Aleksandrov N. Plasma-assisted ignition and combustion. Prog Energy Combust Sci 2013;391:61–110. https://doi.org/10.1016/j.pecs.2012.05.003.

[25] Rajasegar R, Mitsingas CM, Mayhew EK, Yoo J, Lee T. Proper orthogonal decomposition for analysis of plasma-assisted premixed swirl-stabilized flame dynamics. IEEE Trans Plasma Sci 2016;4412:2940–51. https://doi.org/10.1109/TPS.2016.2622687.
[26] Lacoste DA, Moeck JP, Durox D, Laux CO, Schuller T. Effect of nanosecond repetitively pulsed discharges on the dynamics of a swirl-stabilized lean premixed flame. J. Eng. Gas. Turbines Power 2013;13510. https://doi.org/10.1115/1.4024961.
[27] Larsson A, Zettervall N, Hurtig T, Nilsson EJK, Ehn A, Petersson P, et al. Skeletal methane-air reaction mechanism for large eddy simulation of turbulent microwave-assisted combustion. Energy Fuels 2017;312:1904–26. https://doi.org/10.1021/acs.energyfuels.6b02224.
[28] Bak MS, Do H, Mungal MG, Cappelli MA. Plasma-assisted stabilization of laminar premixed methane/air flames around the lean flammability limit. Combust Flame 2012;15910:3128–37. https://doi.org/10.1016/j.combustflame.2012.03.023.
[29] Nagaraja S, Li T, Sutton JA, Adamovich IV, Yang V. Nanosecond plasma enhanced H2/O2/N2 premixed flat flames. Proc Combust Inst 2015;353:3471–8. https://doi.org/10.1016/j.proci.2014.08.024.
[30] Sun J, Tang Y, Li S. Plasma-assisted stabilization of premixed swirl flames by gliding arc discharges. Proc Combust Inst 2020;384:6733–41. https://doi.org/10.1016/j.proci.2020.06.223.
[31] Tang Y, Xie D, Shi B, Wang N, Li S. Flammability enhancement of swirling ammonia/air combustion using AC powered gliding arc discharges. Fuel 2022;313:122674. https://doi.org/10.1016/j.fuel.2021.122674.
[32] Tang Y, Yao Q, Zhuo J, Li S. Plasma-assisted pyrolysis and ignition of pre-vaporized n-heptane, iso-octane and n-decane. Fuel 2021;289:119899. https://doi.org/10.1016/j.fuel.2020.119899.
[33] Cui W, Ren Y, Li S. Stabilization of premixed swirl flames under flow pulsations using microsecond pulsed plasmas. J Propul Power 2019;351:190–200. https://doi.org/10.2514/1.B37219.
[34] S. Pancheshnyi, B. Eismann, G.J.M. Hagelaar, Pitchford LC. Computer code ZDPlasKin; 2008. Available from: http://www.zdplaskin.laplace.univ-tlse.fr. [Accessed 2021/06/27].
[35] Beer JM, Chigier NA. Combustion aerodynamics. Applied Science Publishers; 1974.
[36] Ducruix S, Durox D, Candel S. Theoretical and experimental determinations of the transfer function of a laminar premixed flame. Proc Combust Inst 2000;281:765–73. https://doi.org/10.1016/S0082-0784(00)80279-9.
[37] Zhang C, Shao T, Wang R, Huang W, Niu Z, Schamiloglu E. A repetitive microsecond pulse generator for atmospheric pressure plasma jets. IEEE Trns Dielectr Electr Insul 2015;224:1907–15. https://doi.org/10.1109/TDEI.2014.005042.
[38] Frank JH, Kalt PA, Bilger RW. Measurements of conditional velocities in turbulent premixed flames by simultaneous OH PLIF and PIV. Combust Flame 1999;1161–2:220–32. https://doi.org/10.1016/S0010-2180(98)00041-8.
[39] Kee RJ, Grcar JF, Smooke MD, Miller JA, Meeks E. PREMIX: a Fortran program for modeling steady laminar one-dimensional premixed flames. Sandia National Laboratories Report 1985SAND85-8249.
[40] Tang Y, Zhuo J, Cui W, Li S, Yao Q. Non-premixed flame dynamics excited by flow fluctuations generated from Dielectric-Barrier-Discharge plasma. Combust Flame 2019;204:58–67. https://doi.org/10.1016/j.combustflame.2019.03.003.
[41] Poinsot T, Veynante D. Theoretical and numerical combustion. RT Edwards: Inc; 2005.
[42] Sutherland W. LII. The viscosity of gases and molecular force. The London, Edinburgh, and Dublin Philosophical Magazine and Journal of Science 2009;36223:507-31. https://doi.org/10.1080/14786449308620508.
[43] Jasak H, Jemcov A, Tukovic Z. OpenFOAM: A C++ library for complex physics simulations. International workshop on coupled methods in numerical dynamics. 1000. IUC Dubrovnik Croatia; 2007:1-20.
[44] Bulat G, Fedina E, Fureby C, Meier W, Stopper U. Reacting flow in an industrial gas turbine combustor: LES and experimental analysis. Proc Combust Inst 2015;353:3175–83. https://doi.org/10.1016/j.proci.2014.05.015.
[45] Kazakov A, Frenklac M. Available from: http://combustion.berkeley.edu/drm/. [Accessed 2021/04/23].
[46] Issa RI. Solution of the implicitly discretised fluid flow equations by operator-splitting. J Comput Phys 1986;621:40–65. https://doi.org/10.1016/0021-9991(86)90099-9.
[47] Chterev I, Foley CW, Foti D, Kostka S, Caswell AW, Jiang N, et al. Flame and Flow Topologies in an Annular Swirling Flow. Combust Sci Technol 2014;1868:1041–74. https://doi.org/10.1080/00102202.2014.882916.
[48] Mao R, Wang J, Lin W, Han W, Zhang W, Huang Z. Effects of flow–flame interactions on the stabilization of ultra-lean swirling CH4/H2/air flames. Fuel 2022;319:123619. https://doi.org/10.1016/j.fuel.2022.123619.
[49] Mao X, Chen Q. Effects of vibrational excitation on nanosecond discharge enhanced methane–air ignition. AIAA J 2018;5611:4312–20. https://doi.org/10.2514/1.J057304.
[50] Ehn A, Zhu JJ, Petersson P, Li ZS, Aldén M, Fureby C, et al. Plasma assisted combustion: effects of O3 on large scale turbulent combustion studied with laser diagnostics and Large Eddy Simulations. Proc Combust Inst 2015;353:3487–95. https://doi.org/10.1016/j.proci.2014.05.092.
[51] Dong M, Cui J, Jia M, Shang Y, Li S. Large eddy simulation of plasma-assisted ignition and combustion in a coaxial jet combustor. Energy 2020;199:117463. https://doi.org/10.1016/j.energy.2020.117463.
[52] Phelps. Available from: http://lxcat.com/. [Accessed 2021/04/19].
[53] IST-LISBON. Available from: www.lxcat.net. [Accessed 2021/04/19].
[54] Straub HC, Lin D, Lindsay BG, Smith KA, Stebbings RF. Absolute partial cross sections for electron-impact ionization of CH4 from threshold to 1000 eV. J Chem Phys 1997;10611:4430–5. https://doi.org/10.1063/1.473468.
[55] Castela M, Stepanyan S, Fiorina B, Coussement A, Gicquel O, Darabiha N, et al. A 3-D DNS and experimental study of the effect of the recirculating flow pattern inside a reactive kernel produced by nanosecond plasma discharges in a methane-air mixture. Proc Combust Inst 2017;363:4095–103. https://doi.org/10.1016/j.proci.2016.06.174.
[56] Xu DA, Lacoste DA, Rusterholtz DL, Elias PQ, Stancu GD, Laux CO. Experimental study of the hydrodynamic expansion following a nanosecond repetitively pulsed dischage in air. Appl Phys Lett 2011;9912. https://doi.org/10.1063/1.3641413.
[57] Cho ES, Chung* SH, Oh TK. Local Karlovitz numbers at extinction for various fuels in counterflow premixed flames. Combust Sci Technol 2006;1789:1559–84. https://doi.org/10.1080/00102200500536175.
[58] Chterev I, Emerson B, Lieuwen T. Velocity and stretch characteristics at the leading edge of an aerodynamically stabilized flame. Combust Flame 2018;193:92–111. https://doi.org/10.1016/j.combustflame.2018.02.024.
[59] Tuttle SG, Chaudhuri S, Kopp-Vaughan KM, Jensen TR, Cetegen BM, Renfro MW, et al. Lean blowoff behavior of asymmetrically-fueled bluff body-stabilized flames. Combust Flame 2013;1609:1677–92. https://doi.org/10.1016/j.combustflame.2013.03.009.
[60] Sun J, Ren Y, Tang Y, Li S. Influences of heat flux on extinction characteristics of steady/unsteady premixed stagnation flames. Proc Combust Inst 2020;382:2305–14. https://doi.org/10.1016/j.proci.2020.06.316.
[61] Rusterholtz DL, Lacoste DA, Stancu GD, Pai DZ, Laux CO. Ultrafast heating and oxygen dissociation in atmospheric pressure air by nanosecond repetitively pulsed discharges. J Phys D: Appl Phys 2013;4646. https://doi.org/10.1088/0022-3727/46/46/464010.
[62] Uddi M, Jiang N, Mintusov E, Adamovich IV, Lempert WR. Atomic oxygen measurements in air and air/fuel nanosecond pulse discharges by two photon laser induced fluorescence. Proc Combust Inst 2009;321:929–36. https://doi.org/10.1016/j.proci.2008.06.049.
[63] Weng W, Nilsson E, Ehn A, Zhu J, Zhou Y, Wang Z, et al. Investigation of formaldehyde enhancement by ozone addition in CH4/air premixed flames. Combust Flame 2015;1624:1284–93. https://doi.org/10.1016/j.combustflame.2014.10.021.